

Long-Wavelength Rupturing Instability in Surface-Tension-Driven Bénard Convection

J. B. Swift¹, Stephen J. Van Hook¹, Ricardo Becerril¹, W. D. McCormick¹, H. L. Swinney¹, ¹ Center for Nonlinear Dynamics and Dept. of Physics, The University of Texas, Austin TX 78712, USA, svanhook@chaos.ph.utexas.edu., Michael F. Schatz², ² Georgia Institute of Technology, Atlanta, Georgia 30332. schatz@ranch.physics.gatech.edu.

1 INTRODUCTION

A liquid layer with a free upper surface and heated from below is subject to instabilities due to both thermocapillary and buoyancy forces. While buoyancy is usually dominant in terrestrial convection experiments, thermocapillarity is dominant in microgravity. Using thin liquid layers (< 0.05 cm), one can also achieve thermocapillary-dominated convection in terrestrial experiments. The criterion for determining that an experiment is thermocapillary-dominated is that $M/R > 1$, where the Marangoni number $M = \sigma_T \Delta T d / \rho \nu \kappa$ characterizes the thermocapillary driving and the Rayleigh number $R = \alpha g \Delta T d^3 / \nu \kappa$ characterizes the buoyancy driving (see figure 1 for definitions). In the experiments described in this paper, $M/R \geq 100$.

In the thermocapillary-driven regime, two qualitatively different instabilities can appear --- short-wavelength hexagonal Bénard convection cells [1, 2] and a long-wavelength deformational mode [3, 4, 5]. The hexagonal and long-wavelength instabilities differ in the stabilizing mechanisms that compete with destabilizing thermocapillary effects due to different types of fluctuations [6]. The short-wavelength hexagonal instability originates from temperature fluctuations on the free surface, which initiate thermocapillary flow along the interface; the imposed vertical temperature difference across the liquid layer sustains the flow. Thermal and viscous diffusion, however, dampen the temperature fluctuations and associated fluid flow. Alternatively, the long-wavelength mode originates from fluctuations of the free surface height $h(x, y)$, which cause a temperature variation on the interface because of the imposed temperature gradient. By thermocapillarity, the cool elevated region pulls liquid from the warm depressed region and, if allowed to continue, thermocapillarity would pile all the liquid from one region of the layer into an adjacent region. Gravity, though, attempts to flatten the interface and thus to stabilize these deformational perturbations. In addition, surface tension selects a long-wavelength for this deformational instability since surface tension resists curvature of the interface and thus stabilizes long wavelength modes least.

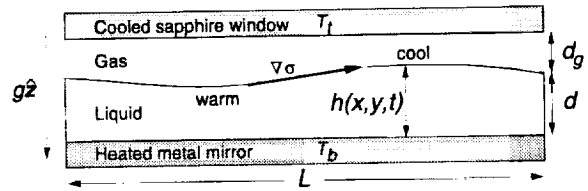


Figure 1: Sketch of surface-tension-driven Bénard (Marangoni) convection cell of horizontal extent $L = 3.81$ cm, mean liquid depth $d \sim 0.01$ cm, mean gas depth $d_g \sim 0.03$ cm, and local interface position $h(x, y, t)$. There is a mean temperature different ΔT across the liquid layer. The liquid has surface tension σ , temperature coefficient of surface tension σ_T , kinematic viscosity ν , thermal diffusivity κ , and thermal expansion coefficient α .

2 LINEAR THEORY

The linear stability analysis for the short-wavelength mode was first published by Pearson [1] and the stability analysis for the full problem, including the long-wavelength mode, was first published by Smith [4]. The hexagonal mode appears at wavenumber $q = 2$ (nondimensionalized by d) when

$$M_c \approx 80 \left(1 + \frac{k_y}{k} \right), \quad (1)$$

where k and k_y are, respectively, the liquid and gas thermal conductivities. The long-wavelength mode appears at wavenumber $q = 0$ at $M_c = 2G/3(1 + F)$, where

$$F \equiv \frac{d}{d_g} \left(\frac{1 - \frac{k_y}{k}}{1 + \frac{dk_y}{kd_g}} \right) \quad (2)$$

characterizes heat transport at the interface. In a real experiment of horizontal extent L , the long-wavelength mode occurs at $q_0 = 2\pi d/L$ and

$$M_c = \frac{2G}{3(1 + F)} + \frac{q_0^2}{C}, \quad (3)$$

where $C = \rho \nu \kappa / \sigma d$ is the capillary number. The instability seen in a given experiment corresponds to the smaller of the M_c in equations (1) and (3). While $G \rightarrow 0$

in microgravity, and thus the long-wavelength mode would be the primary instability in an experiment of very large aspect ratio ($q_0 \rightarrow 0$), the Benard hexagons can still be the primary instability in a finite-aspect ratio system. For example, experiments on Benard convection aboard Apollo 14 [7] and Apollo 17 [8] yielded short-wavelength Benard convection cells and not the long-wavelength instability, even though $G < 1$. In the Apollo experiments, the aspect-ratio correction (q_0^2/C) shifted the onset of the long-wavelength mode to $M \sim 280$, above the onset of hexagons.

3 NONLINEAR THEORY

To examine the nonlinear stability and behavior of the long-wavelength instability, we have derived an evolution equation for the interface height $h(x, y, t)$ from the Navier-Stokes equations in the limit of long wavelength disturbances[6]:

$$\frac{\partial h}{\partial t} + \nabla \cdot \left\{ \frac{3D}{2} \frac{h^2 \nabla h}{f(F, h)} - h^3 \nabla h + \frac{h^2}{B} \nabla^2 \nabla h \right\} = 0, \quad (4)$$

where the domain of both x and y is $[0, 2\pi]$, $f(F, h) \equiv (1 + F - Fh)^2 / (1 + F)$, $D \equiv M/G$ is the inverse dynamic Bond number, and $B = GC/q_0^2$ is the static Bond number. The first term in curly brackets describes the effect of thermocapillarity; the second, gravity; and the third, surface tension. Equation (4) reduces to the evolution equations of Davis[9, 10] and Oron & Rosenau[11] in the limit of $F = 0$ ($d_g/d \rightarrow \infty$, or $k = k_g$). The linear stability analysis of this equation agrees with Smith [4] for $q_0 \ll 1$.

To determine the nature of the bifurcation, we perform a weakly nonlinear analysis of the evolution equation (4) by considering just the two lowest order wavenumbers in the deformation $\eta \equiv h - 1$; we assume that the lowest order $\eta_1 \approx |\epsilon|^{1/2}$, where $\epsilon \equiv (M - M_c)/M_c$, the second lowest order $\eta_2 \approx |\epsilon|$, and all higher orders of η go as the 3/2 or higher power of $|\epsilon|$. The bifurcation is found to be subcritical (a backwards pitchfork) for all parameters. In addition, the signs of the second and higher order modes (η_2 , etc.) change at $F = 1/2$, hinting at the qualitative difference in solutions that we will describe later for $F < 1/2$ and $F > 1/2$.

Equation (4) can also be solved to find all the one-dimensional steady states $h(x)$; The solutions we find agree with the weakly nonlinear analysis for small $|\epsilon|$; the bifurcation curve continues backwards in ϵ until it terminates because the solutions represented cease

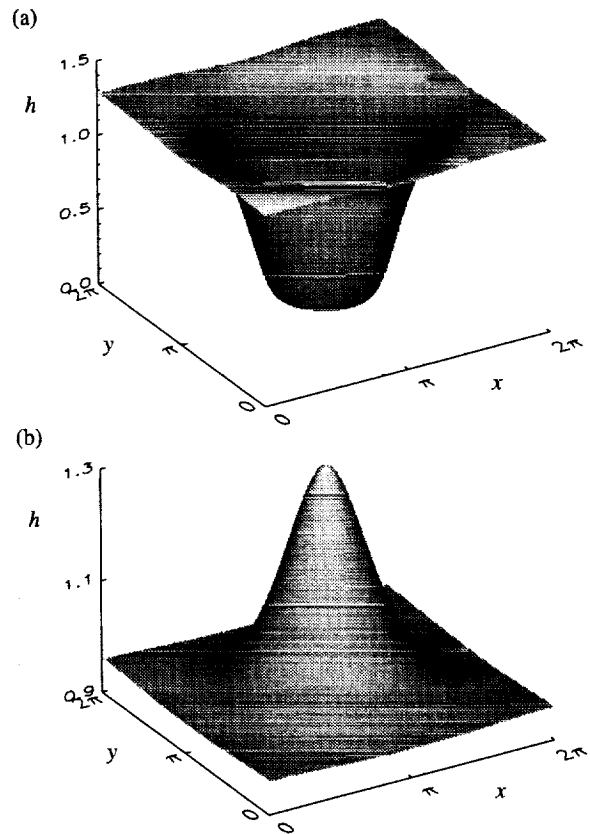


Figure 2: Two-dimensional profile of long-wavelength mode just before rupture for 5% above linear instability. (a) Dry spot with $F = 1/3$ and $B = 30$, (b) High spot with $F = 2/3$ and $B = 30$.

to become physical. Nowhere does the bifurcation curve turn over in a saddle-node bifurcation and form a stable branch. The unstable solutions on the bifurcation curve appear differently for $F < 1/2$ and $F > 1/2$; for $F < 1/2$, the solutions are localized depressions and for $F > 1/2$ the solutions are localized elevations. Oron and Rosenau [11] performed a similar analysis for $F = 0$ and also found no stable solutions.

We numerically simulate (4) with both one- and two-dimensional interfaces. We use a spectral method in order to enforce the continuity condition, which in one dimension is $\int_0^{2\pi} (h - 1) dx = 0$. Fourier series are the natural basis function since we use periodic boundary conditions, and Fourier series automatically satisfy continuity. The simulation employs a pseudospectral method to handle the nonlinear terms. Because of the fourth-order nonlinearity, a 2/5 rule (equivalent to the 2/3 rule for quadratic nonlinearities) is required to prevent aliasing --- e.g., for 128 spatial locations, only 51 spectral modes q from -25 to +25 are used. At each time-step, the power in the remaining 3/5 of modes is set to zero.

A dry spot forms for $F < 1/2$ (figure 2 a), while for $F > 1/2$ a high spot forms, which physically would pop up to the top plate (figure 2 b). Thus, the prediction of weakly nonlinear and potential theory of a change at $F = 1/2$ is observed in the simulations. The structure of the dry or high spot does not depend strongly on F far from $F = 1/2$, though the size depends on the static Bond number B , which gives the relative strengths of gravity and surface tension. High surface tension (B small) prevents sharp structures from forming, while a low surface tension (B large) allows the formation of sharp structures. As predicted by the nonlinear analyses, no stable, deformed states before rupture are seen in either one or two dimensions. After rupture, the dry spot eventually saturates, though this phenomenon is not captured by the evolution equation since as $h_{min} \rightarrow 0$, the power in the higher order modes begins to dominate, spectral convergence is lost, and the simulation breaks down.

4 EXPERIMENTAL DESIGN

The liquid lies on a 3.81-cm-diameter, gold-plated aluminum mirror (see figure 3). The mirror is attached to an aluminum plate whose bottom is heated by a 14 Ω thin-film resistance heater. A thermistor in the center of the aluminum plate measures T_b . A cooled, 3-mm-thick sapphire window bounds the gas from above. Chloro-

form is employed as the cooling fluid to allow imaging with an infrared (3-5 μm) camera. Cooled chloroform is pumped between two sapphire windows and then through a heat exchanger that maintains the temperature of the chloroform at 21.3 ± 0.1 $^\circ\text{C}$.

The total gap ($d + d_g$) between the lower sapphire window and the mirror bottom is uniform to 10 fringes (3.2 μm), as verified interferometrically. The size of the gap is determined by introducing indium shims of various sizes and observing the change in the interference fringes between the window and the mirror. We consider the gap to have the same thickness as the shim when the shim does not perturb the fringes, but a slightly thicker shim (by 5 μm) does.

An aluminum sidewall laterally constrains the liquid. The liquid depth is uniform to a fringe (0.32 μm) in the central 75% of the cell at $\Delta T = 0$. The depth is measured using a stylus attached to a micrometer. The position of the upper interface is determined when the liquid suddenly wets the sharp tip of the stylus as the stylus is lowered. The stylus is then lowered further until contact with the mirror is signaled by an ohmmeter connected to the stylus and the metal mirror. The liquid depths can be measured to ± 5 μm .

For most experiments we use a $\nu = 0.102$ Stoke (at 50 $^\circ\text{C}$) silicone oil that has been distilled once to remove low vapor pressure components, which can condense on the cool, upper plate [12]. Infrared images are made using an infrared-absorbing (at 4.61 μm with an extinction length of order a few microns) polymethylhydrosiloxane silicone oil with $\nu \approx 0.25$ Stoke at 50 $^\circ\text{C}$.

Liquid depths range from 0.007 to 0.027 cm. Gas layer thicknesses range from 0.02 to 0.10 cm. The gas in the upper layer is typically air, although a few experiments employ helium gas. We used helium since it has a much larger thermal conductivity than that of air and thus allows varying F without varying d or d_g .

We use an optical system that serves as both an interferometer and a shadowgraph. When the deformation is small, we use the optical system as an interferometer to give an indication of the deformation of the interface. The mirror-window fringes are much stronger than the mirror-liquid fringes, so it is difficult to count the mirror-liquid fringes to get a quantitative measure of the deformation. When the deformation is large, we use the optical system as shadowgraph, where deformation acts as a lens to focus the incident light. The initial formation of a localized depression is signaled by a bright spot on the shadowgraph image. Once the interface is significantly deformed (as the liquid is in the process of forming a dry or high spot), the deformation can be seen

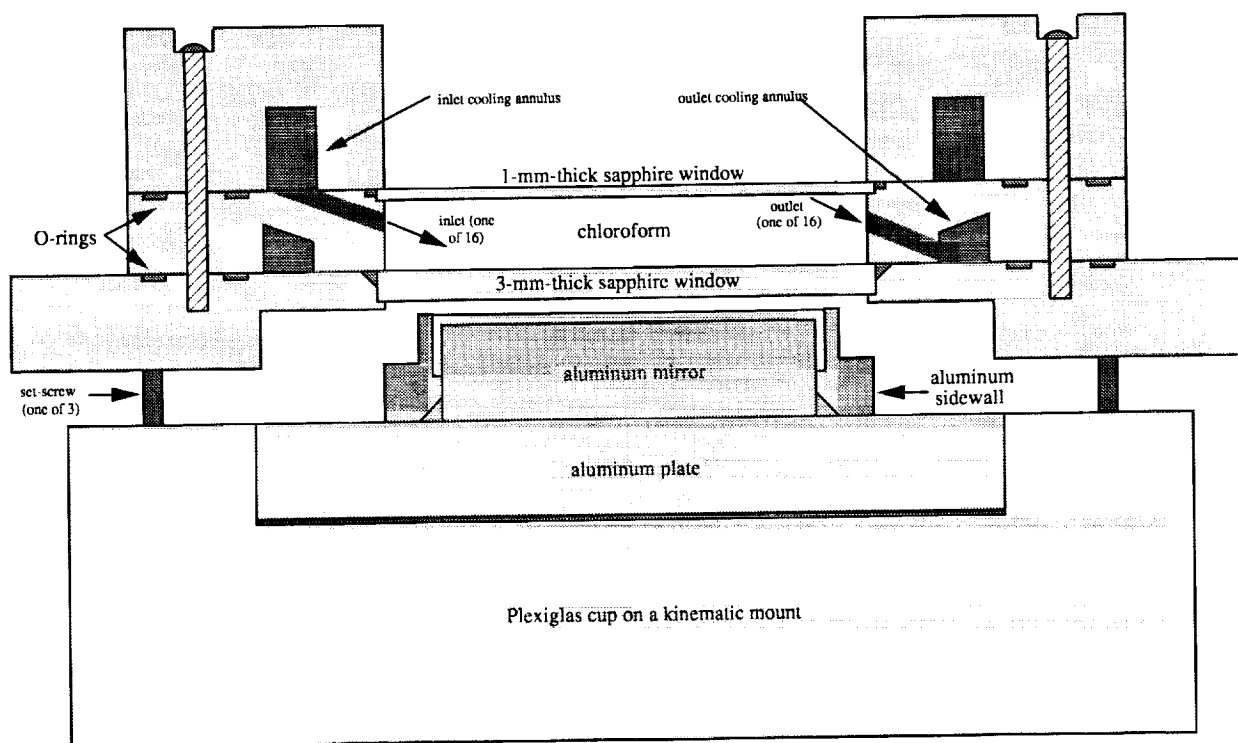


Figure 3: Cross-section of experimental apparatus. Both top and bottom plates are thermally conducting relative to the liquid and gas.

by eye. For making images used in this paper, we employed a 256 × 256 pixel Amber Engineering Proview 5256 LN₂-cooled InSb infrared staring array sensitive in a 0.08 μm band centered around 4.61 μm.

5 EXPERIMENTAL RESULTS

We see four distinct states at onset of instability: the two long-wavelength modes of dry spots (figure 4a) and high spots (figure 4b), a mixed long-wavelength and hexagonal state (figure 4c), and hexagons (figure 4d).

We observe three of these states at the onset of instability for $F < 1/2$. For large G (independent of F), Benard hexagons form (figure 4d). For small G , the long-wavelength dry spot forms (figure 4a). For intermediate G , both the long-wavelength (dry spot) and hexagonal modes appear together (figure 4c). In this case, the long-wavelength deformational mode is linearly unstable and its formation induces the formation of the hexagonal mode by increasing the local depth in the region surrounding the dry spot. The horizontal extent of the dry spot is $\sim 100d$ and the area of the dry spot is typically $1/4 - 1/3$ the area of the entire cell. Once the dry spot forms, fluid flow consists of steady-

state convection concentrated at the edge of the dry spot.

As predicted by nonlinear theory, for $F > 1/2$ the liquid layer forms a high spot (figure 4d), where the liquid pops-up to the top plate (sapphire window).

Since the time-scale of formation of the hexagons is the vertical diffusion time ($d^2/\kappa \approx 0.1$ s), while the time-scale for the long-wavelength mode is the horizontal diffusion time ($L^2/\kappa \approx 3$ hours), quickly ramping the temperature above $M = 80$ allows formation of the hexagons as the primary instability even when the long-wavelength instability would be primary if ΔT were increased quasistatically, as assumed by linear theory. If ΔT is then decreased slowly below onset of hexagons, a dry spot can form once the hexagons have disappeared.

A comparison of the experimental measurements of onset to linear stability theory is given in figure 5. The linear stability theory assuming periodic boundary conditions (the dotted line in figure 5) gives good agreement with the experiments for deep liquid depths ($d \gtrsim 0.015$ cm), but poor agreement for shallow liquid depths. Much of the deviation of theory from experiment is due to sidewall effects, both the pinning of the liquid at the sidewalls and under- or over-filling of the liquid. The experiments used a fixed sidewall height of 0.02 cm, so experiments with thinner depths were underfilled

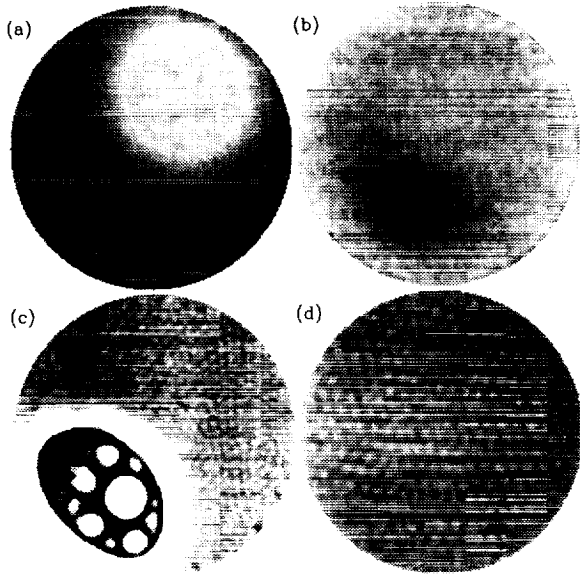


Figure 4: Infrared images of states seen in the experiment. (a) a dry spot ($d = 0.025$ cm, $F = -0.06$). (b) a high spot ($d = 0.037$ cm, $F = 0.91$). (c) dry spot with hexagons in the surrounding region ($d = 0.025$ cm). (the dry spot looks cold the camera sees through the infrared-absorbing liquid to the mirror, which appears cold in the infrared); (d) hexagons ($d = 0.045$ cm, $G = 370$).

and experiments in thicker depths were overfilled. The presence of sidewalls of height different from the mean liquid depth led to an initially deformed interface, even for no imposed temperature gradient. To examine the effects of the sidewalls, we solved equation (4) using non-periodic boundary conditions with Chebyshev polynomials as our basis functions. The boundary conditions used corresponded to pinning of the liquid surface at the sidewall and no net liquid flux through the sidewalls; these boundary conditions automatically satisfied the conservation of liquid condition. The curved, solid line in figure 5 shows the comparison of the experiments with the new theoretical prediction [13]. The quantitative agreement is much better than with periodic boundary conditions, though the agreement is still not exact.

6 CONCLUSION

Two modes of instability exist in surface-tension-driven Benard-Marangoni convection where the liquid is heated from below and cooled from above. The short-wavelength

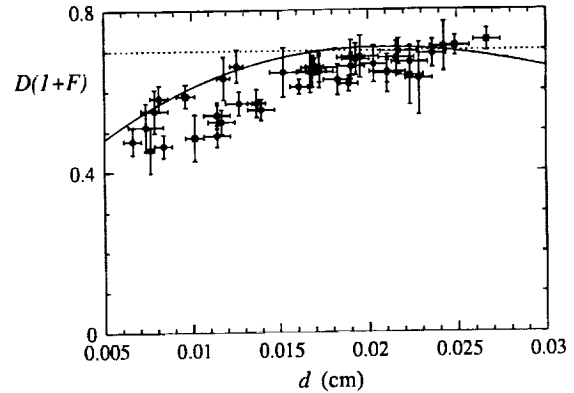


Figure 5: Comparison of instability onset with the predictions of linear stability theory. The prediction of linear stability theory assuming periodic boundary conditions is given by the dashed line at 0.70. This theory gives good agreement with the experiments for thick liquid depths, but there is a significant departure for thin depths. The prediction of linear stability theory including the sidewall effects is given by the curved solid line.

hexagonal mode ($q = 2$) occurs for large G , when diffusion is the important (slow) stabilizing mechanism. The long-wavelength deformational mode ($q = 2\pi d/L \ll 1$) occurs for small G , when gravity is the important (slow) stabilizing mechanism. This long-wavelength instability can take the form of either a localized depression that evolves to a dry spot, or a localized elevation (high spot) that accelerates upwards and causes the liquid to pop up to the top plate. The relative thicknesses and thermal conductivities of the liquid and gas layers determine whether the dry spot or high spot forms; a high spot forms where the liquid thermal conductivity is much larger than the gas thermal conductivity and the liquid depth is nearly equal to or greater than the gas depth. The deformation due to the long-wavelength mode can cause the formation of the hexagonal mode by increasing the local value of M above the critical value for the hexagons.

The long-wavelength instability is described by an evolution equation for the height of the interface. Analysis of the evolution equation predicts that the instability is subcritical and that the unstable, backwards branch of the bifurcation curve never turns over to a stable branch. Numerical simulations of the evolution equation reveal dry spot and high spot states that agree qualitatively with what is seen in the experiment. Linear stability theory using periodic boundary conditions works well when the interface is initially flat; however,

when the interface is deformed, the deformation much be included in the theory to predict the correct onset.

This research is supported by the NASA Microgravity Science and Applications Division (Grant No. NAG3-1839), the Office of Naval Research (Grant No. N00014-89-J-1495), and a NASA ESS Cooperative Agreement (NCCS5-154).

References

- [1] J. R. A. Pearson, *J. Fluid Mech.* **4**, 489 (1958).
- [2] M. F. Schatz, S. J. VanHook, W. D. McCormick, J. B. Swift and H. L. Swinney, *Phys. Rev. Lett.* **75**, 1938 (1995).
- [3] L. E. Scriven and C. V. Sternling, *J. Fluid Mech.* **19**, 321 (1964).
- [4] K. A. Smith, *J. Fluid Mech.* **24**, 401 (1966).
- [5] S. J. Van Hook, M. F. Schatz, W. D. McCormick, J. B. Swift, and H. L. Swinney, *Phys. Rev. Lett.* **75**, 4397 (1995).
- [6] S. J. Van Hook, M. F. Schatz, J. B. Swift, W. D. McCormick, and H. L. Swinney, *J. Fluid Mech.* **345**, 45 (1997).
- [7] P. G. Grodzka and T. C. Bannister, *Science* **176**, 506--508 (1972).
- [8] P. G. Grodzka and T. C. Bannister, *Science* **187**, 165 (1975).
- [9] S. H. Davis, in *Waves on Fluid Interfaces*, edited by R. E. Meyer (Academic Press, New York, NY, 1983), p. 291.
- [10] S. H. Davis, *Annu. Rev. Fluid Mech.* **19**, 403 (1987).
- [11] A. Oron and P. Rosenau, *J. Phys. II (France)* **2**, 131 (1992).
- [12] M. F. Schatz and K. Howden, *Exp. Fluids* **19**, 359 (1995).
- [13] R. Becerril, S. J. Van Hook, and J. B. Swift, submitted to *Phys. Fluids* (1998).